ACS OMEGA

Open Access

http://pubs.acs.org/journal/acsodf

Article

Microscopic Particle Image Velocimetry Analysis of Multiphase Flow in a Porous Media Micromodel

Md. Abdul Karim Miah, Kawkab Ahasan, Todd A. Kingston, Michael G. Olsen,* and Jaime J. Juárez*

Cite This: *ACS Omega* 2024, 9, 34070−34080

Read Online

ACCESS | Metrics & More | Article Recommendations | Supporting Information

ABSTRACT: Pore-scale oil displacement behavior was investigated in a porous media micromodel using microscopic particle image velocimetry (μPIV). Porous media micromodels consisting of an ordered square array of cylindrical pillars with 50 and 70% porosities were fabricated with photolithography. The oil displacement was performed with the injection of water at flow rates of 37.5, 75, and 150 μL/h. These flow rates correspond to Reynolds number of 1.1×10^{-2}, 2.2×10^{-2}, and 4.4×10^{-2}, respectively in the 50% porous channel, and 1.84×10^{-3}, 3.69×10^{-3}, and 7.38×10^{-3}, respectively in the 70% porous channel. The capillary numbers for these flow rates are 2.18×10^{-5}, 4.36×10^{-5}, and 8.72×10^{-5}, respectively in the 50% porous channel, and 1.56×10^{-5}, 3.12×10^{-5}, and 6.23×10^{-5}, respectively in the 70% porous channel. The micromodel is initially saturated with oil, with the invading water phase following the path of least resistance as it displaces the oil. The μPIV data were used to construct probability density functions (PDFs) which show an initial, nonzero, peak in transverse velocity as the water enters the micromodel. The PDFs broaden with time, indicating that the water is spreading, before retracting to a peak velocity of 0 mm/s, indicating that the water displacement has achieved equilibrium. We developed a model based on conservation of mass to describe the efficiency of the displacement process. All flow conditions demonstrate peak displacement efficiency when the amount of oil phase displacement is ∼9 pore volumes in 50% porous channel and ∼4 pore volumes in 70% porous channel.

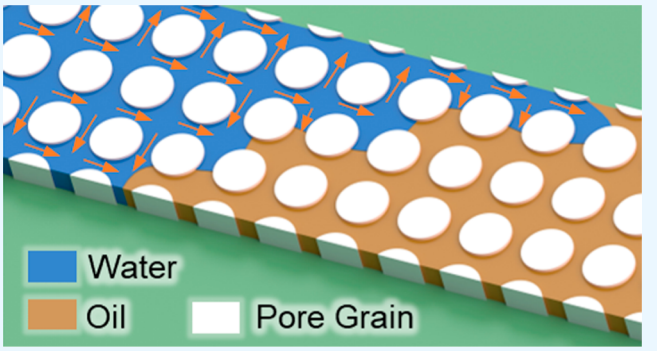

1. INTRODUCTION

A fundamental understanding of fluid flow through porous media is important for a wide range of applications, including the recovery of natural resources,[1] modeling of transport phenomena in biological tissues,[2] and mitigating the transport of pollutants to groundwater.[3] One challenge in understanding fluid flow through porous media lies in characterizing the path a fluid will follow as it passes through the medium. Typically, the flow will traverse a path that minimizes the hydraulic resistance to the fluid.[4] However, the fluid path is affected by a variety of factors such as the structural complexity of the porous media[5] or the interfacial tension of the fluid.[6] Understanding how such factors influence flow through porous media would improve our ability to predict and control transport processes in porous media. Thus, there is a need to identify new approaches for fluid flow characterization in porous media.

Flow characterization in porous media begins with the development of porous media micromodels that mimic the structure of naturally occurring pores. The earliest micromodels utilized glass beads packed inside of a microchannel as a mimic for porous media.[7] This approach to micromodel fabrication has the advantage of being simple to implement. However, the distribution of glass beads in these types of micromodels is random, thus making it difficult to identify how the inherent randomness of the micromodel structure affects the flow profile. Photolithography has emerged as an alternate tool for micromodel fabrication due to its allowing for the precise control of the micromodel structure. Furthermore, with photolithography, a wide range of optically clear materials are available for micromodel fabrication, including polydimethylsiloxane (PDMS),[8] photoresist,[9] and Norland optical adhesive.[10]

The optical transparency of micromodels fabricated using the materials described above enables the systematic study of flow characteristics inside the pore structures. For example, microscopic particle image velocimetry (μPIV) is a velocity measurement and flow visualization technique that serves as the basis for many porous media micromodel studies. This technique relies on capturing images of the displacement of seed particles in sequential video frames and using that

Received: May 16, 2024
Revised: July 2, 2024
Accepted: July 18, 2024
Published: July 24, 2024

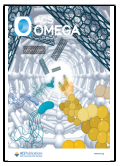

displacement to calculate local flow velocity. The earliest μPIV studies of porous media micromodels utilized a fluid that was matched to the refractive index of the porous media micromodel, eliminating optical distortion due to refraction and allowing for the imaging of flow structures deep into the micromodel[11] and for the measurement of 3D velocity profiles.[12] In microchannels with rectangular cross section, μPIV can be used without the need to match indices of refraction, and such microchannels have been used to investigate the velocity distribution in micromodels containing cylindrical pillars designed to mimic natural media.[13]

μPIV has been used to characterize a variety of porous media process features aside from local velocity fields. Seed particles dispersed in a wetting medium can be used to monitor its drainage (i.e., wetting phase displacement) in the presence of a displacing nonwetting phase.[14] These types of μPIV experiments provide a way to directly investigate interfacial conditions in two-phase porous media flow, providing evidence of slip conditions at fluid−fluid interfaces during the displacement process.[15] The drainage process can leave ganglia (i.e., blobs) of wetting fluid trapped within the pores. Ganglia exhibit internal circulation patterns that vary based on the capillary number of the flow.[16] μPIV can also provide insight into dynamical processes such as Haines jumps, where the pressure builds at the fluid−fluid interface within the pore.[17] The interface will break once a critical pressure is reached, causing an invading fluid to fill a pore in a momentary burst of fluid velocity.

The work presented here examines the dynamics of oil phase displacement by a water phase in porous media micromodels. These results have direct application to processes such as enhanced oil recovery that rely on using water to displace oil from porous rock. The novelty of this work lies in the capability to dynamically visualize and quantify the displacement process from the initial point of water phase invasion until the displacement reaches equilibrium within the observed field of view. The results show that the rate of displacement can be described through a modified conservation of mass model. Further, the authors also define a flow displacement efficiency to compare the displacement process across different flow rates and find that these displacement efficiencies peak once the fluid has displaced approximately nine pore volumes for micromodels with 50% porosity and four pore volumes for micromodels with 70% porosity. The experimental and analysis techniques presented here can form the basis for investigating and analyzing a variety of porous media displacement processes from the extraction of natural resources to chemical processing in packed bed reactors.

2. MATERIALS AND METHODS

2.1. Micromodel Preparation. The porous media micromodel was prepared using conventional soft lithography techniques. The process begins by using AUTOCAD to create a drawing of a porous media micromodel. Two micromodels, one with 50% porosity and another with 70% porosity, were used in this work. An example device with 70% porosity is shown in Figure 1. In this example device, 30% of the available volume is occupied by multiple cylindrical pillars that act as pore grains, each with a diameter of 300 μm. The in-plane dimensions of the device, 1.7 mm wide and 17 mm long, were chosen such that the channel would fit on a standard glass slide (the out-of-plane dimension is determined by the thickness of the photoresist, as described later in this section). The CAD

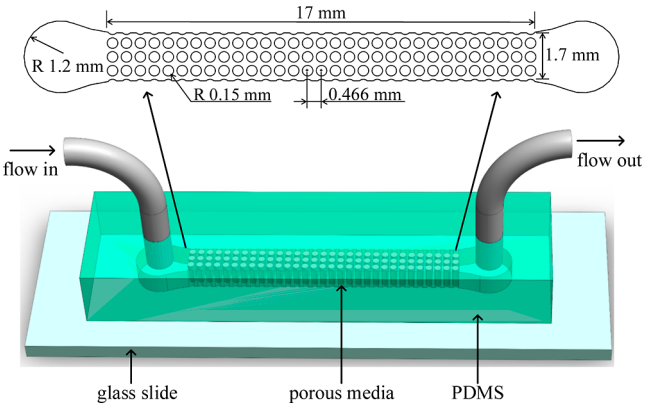

Figure 1. Schematic of the porous media micromodel with 70% porosity used in this work. The dimensions of the device are shown in the inset above.

file for the micromodel was printed on an optically clear photomask by Fineline Imaging, Inc.

The micromodel pattern was transferred to a silicon wafer using photolithography. In this process, SU-8 2050 photoresist was poured onto a 100 mm-diameter silicon wafer (University Wafer, catalog # 452) which was spun at high speed to spread the photoresist evenly across the surface. The parameters for the process, including spin rates, baking times, and UV energy exposure, are shown in Table 1. These parameters produce a

Table 1. Parameter Values for Soft Lithography

photoresist	SU-8 2050
thickness	50 ± 3.2 μm
spin coating (RPM and time)	500 rpm for 5 s at acceleration of 100 rpm/s 3000 rpm for 35 s at acceleration of 300 rpm/s
soft bake times	3 min at 65 °C and 7 min at 95 °C
exposure energy	195 MJ/cm^2
post exposure bake times	2 min at 65 °C and 8 min at 95 °C

50 μm film of uniform thickness across the wafer surface. After the post exposure bake was completed, the wafer was placed in SU-8 developer for about 3 min to stabilize the pattern.

The micromodel was molded using PDMS to create the device used in experiments. The PDMS was prepared by stirring PDMS monomer together with the curing agent in a ratio of 10 to 1. Bubbles were removed using a vacuum chamber before the PDMS was poured into a Petri dish containing the wafer with the pattern. The Petri dish containing the PDMS was heated to 42 °C for 5 h to allow the PDMS to cross-link. A razor was used to cut the PDMS containing the mold of the channel from the wafer.

Biopsy punches were used to create inlet and outlet holes in the reservoirs at either end of the channel to allow for the passage of fluid through the device. The PDMS mold with the channel was placed face up with a glass slide (Fisher Scientific, catalog # 12-550-A3) in plasma chamber (Harrick Plasma, PDC-32G) and exposed to plasma at the highest radio frequency setting for 40 s. The mold and glass slide were pressed together immediately after plasma exposure. To strengthen the bond between the PDMS and glass slide, the device was heated to 100 °C for 10 min. The micromodel was completed by inserting 2.38 mm diameter (0.8 mm inner diameter) silicone tubes (U.S. Plastics, catalog # 57286) into

https://doi.org/10.1021/acsomega.4c04680
ACS Omega 2024, 9, 34070−34080

the reservoir inlet and outlet holes. A small amount of PDMS was poured around the holes to improve the seal.

2.2. Fluid Sample Preparation. Fluorescent polystyrene particles (ThermoFisher Scientific, catalog #F8852) with 1 μm diameter were used as seed particles for the μPIV experiments. The Stokes number for the highest flow rate used in the presented experiments was approximately 4.3×10^{-6}, indicating the seed particles will accurately follow the fluid streamlines, thus making these particles ideal for characterizing the flow field in the porous media micromodel.[18,19] Fluorescent tracer particles were added to the water phase at a concentration of 0.05% by volume. The oil phase consisted of 25 cSt mineral oil purchased without modification from ASI Standards (catalog # MVMO25).

The water phase has a viscosity and density of ~1 cSt, and ~1000 kg/m^3, respectively, while the mineral oil has a viscosity and density of 25 cSt, and 853.5 kg/m^3, respectively. The deionized water has no salinity. The interfacial tension of water and oil is 10.05 mN/m.

2.3. Experimental Procedures. μPIV experiments were performed using an inverted fluorescent microscope (Olympus IX71). The inlet of the porous media micromodel was connected to syringe pump (Chemyx, Fusion Touch Series model 740) through silicone tubing that interfaced via a 1/16″ nylon barb with the tubing that was inserted into the inlet hole. Tubing was also added to the outlet port on the opposite side of the micromodel. The tubing used for the outlet was long enough to dispense outgoing fluid into a glass beaker that served as a fluid collector. The shortest possible length of tubing was used to minimize the impact of hydraulic capacitance in the experiments.

The experiments begin with injecting up to 8 mL of mineral oil through the system to saturate the porous media micromodel with the mineral oil. This amount of oil fills the tubing, which takes up most of the volume, and the micromodel device. Water injection begins once the saturation procedure is complete. Displacement experiments are performed at three flow rates: 37.5, 75 and 150 μL/h. The capillary number of the displacement process may be calculated from the flow rate as

$$\mathrm{Ca} = \frac{\mu u_0}{\gamma} \tag{1}$$

where μ is the viscosity of the invading fluid, γ is the surface tension of the oil−water system, and u_0 is the interstitial fluid velocity defined[20] as $u_0 = Q/A_c\varphi$, where Q is the flow rate, A_c is the channel cross sectional area, and φ is the device porosity. For 50% porosity, the capillary numbers corresponding to these flow rates are 2.18×10^{-5}, 4.36×10^{-5}, and 8.72×10^{-5}, respectively. For 70% porosity, the capillary numbers corresponding to these flow rates are 1.56×10^{-5}, 3.12×10^{-5}, and 6.23×10^{-5}, respectively To find the interfacial tension between oil and water, the pendant drop method was employed using open sourced software Opendrop.[21] The pendant drop method entails acquiring a silhouette of an axisymmetric fluid droplet and iteratively fitting the Young−Laplace equation to strike a balance between the drop's gravitational deformation and the drop's repairing interfacial tension.[22] The image acquisition was performed using a cell phone (iPhone 13). Our usage of a cell phone camera to image the drop is based on a procedure suggested in the literature.[23] The interstitial fluid velocity may also be incorporated into our definition of the Reynolds number, which is

$$\mathrm{Re} = \frac{\rho u_0 l_0}{\mu} \tag{2}$$

where ρ is the density of the invading fluid and $l_0 = d_0\left[\frac{1}{4}\sqrt{\pi/\varphi} - \frac{1}{2}\right]$ is the pore throat size (i.e., distance between cylinders) for a square array of cylindrical obstacles with d_0 being the obstacle diameter.[24] Using this definition, for 50% porosity, the Reynolds numbers corresponding to these flow rates are 1.1×10^{-2}, 2.2×10^{-2}, and 4.4×10^{-2}, respectively. And, for 70% porosity, the Reynolds numbers corresponding to these flow rates are 1.84×10^{-3}, 3.69×10^{-3}, and 7.38×10^{-3}, respectively, thus ensuring that all experiments were performed in the creeping flow regime.

Figure 2 shows a diagram of the experimental setup. The porous media micromodel was illuminated using a Xenon arc

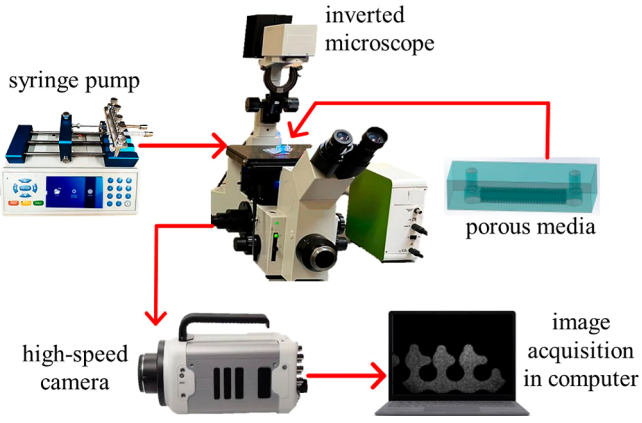

Figure 2. A schematic showing the experimental setup used for μPIV experiments in porous media micromodels.

lamp (75 W) to excite the μPIV seed particles in the water phase. Light from the lamp passes through an excitation filter and is reflected by a dichroic mirror. This mirror directs the excitation light through the objective lens to the specimen, exciting fluorescent particles. These particles emit light at a longer wavelength, which travels back through the objective lens, passes through the dichroic mirror, and goes through the emission filter, blocking any remaining excitation light. Finally, the light reaches the camera. Flow imaging was performed using a Photron FASTCAM Nova S9 high speed camera (1024 × 1024 frame dimensions, 2.0 μm/pixel) with a 10× magnification, 0.3 numerical aperture microscope objective for capturing the images. Photron FASTCAM Viewer software (version 4.0.6.0) was used for image acquisition. Images were captured at a rate of 500 frames per second and at the shutter speed of 1/2000 s.

The video images collected were preprocessed using image masks to exclude unwanted regions of video. Specifically, it was found that the presence of pillars in the images, in which seed particles were absent, contributed to the generation of spurious vectors. Image analysis to determine time-resolved instantaneous velocity fields was performed using the open-sourced software PIVlab − Digital Particle Image Velocimetry Tool for MATLAB.[25] This software utilizes a fast Fourier transform window deformation approach to perform cross-correlation analysis that constructs the velocity fields. A multipass interrogation procedure was used with a final interrogation spot area of 32 pixels by 32 pixels with a step size of 16 pixels

https://doi.org/10.1021/acsomega.4c04680
ACS Omega 2024, 9, 34070−34080

between adjacent interrogation spots (i.e., 50% overlap between adjacent interrogation spots). Standard correlation robustness was used.[26] An in-plane spatial resolution of 32.3 μm was used in the final vector map. The out-of-plane spatial resolution for the experiment was found to be 25 μm.[27−29] Based on the conditions in our experiment, we estimate that the standard error associated with Brownian motion is ∼1.2%. Details on the calculation of this result may be found in Supporting Information.

2.4. Theory. A conservation of mass analysis of the imaged region of interest (ROI) was performed to characterize the rate of oil displacement. This analysis begins by characterizing the ROI as a fixed Eulerian frame of reference. In this context, the rate change in oil volume (V_0) is balanced by the oil phase flux (J_0) as it exits the ROI

$$\frac{dV_0}{dt} = -J_0 \tag{3}$$

In their Supporting Information document, Yeh and Juarez showed that this conservation of mass analysis can be expressed on the basis of saturation[30]

$$\frac{dS_0}{dt} = -rS_0 \tag{4}$$

where $S_0 = A_0/A_t$ is the oil saturation defined as the instantaneous area occupied by the oil within the ROI normalized by the total ROI area. The parameter, $r = u_{avg}/\varphi h$, is a rate constant where u_{avg} is the average velocity of the invading phase in the absence of obstacles (i.e., when porosity is unity), φ is the micromodel porosity, and h is the channel height.

The relationship between water and oil saturation can be obtained through a saturation balance that represents all the phases present in the porous media[31]

$$S_w + S_0 + S_{or} = 1 \tag{5}$$

where S_w is the water saturation and S_{or} represents the irreducible oil saturation (i.e., the amount of oil that cannot be displaced by water invasion). For simplicity, one can define $S_{max} = 1 - S_{or}$ as the maximum achievable water phase saturation. Combining these relationships with eq 4 yields

$$\frac{dS_w}{dt} = r(S_{max} - S_w) \tag{6}$$

which describes the change in water saturation as a function of time. Multiplying both sides of eq 6 by the total area

$$\frac{dA_w}{dt} = r(A_{max} - A_w) \tag{7}$$

leads to an expression that describes how the water phase displaces oil over an area A_w until it reaches an equilibrium point, A_{max}, beyond which the water will no longer displace oil within the ROI. Equation 7 forms the basis for the parameter the authors describe as displacement efficiency

$$\varepsilon = \frac{h}{Q}\frac{dA_w}{dt} \tag{8}$$

where Q is the volumetric flow rate of the water phase. This metric may be used to describe the temporal effectiveness of the water phase displacement process.

Our analysis of the displacement process in the Results and Discussion section suggests that data deviates from the behavior predicted by eq 7. The displacement process appears to be better described by a modified version of eq 7

$$\frac{dA_w}{dt} = nrt^{n-1}(A_{max} - A_w) \tag{9}$$

where n is an adjustable parameter that describes the impact that flow capacitance (i.e., changes in local volume) have on the displacement process. Integrating eq 9 with respect to time yields an expression that describes how the area displaced by the water changes with time

$$A_w(t) = A_{max}(1 - e^{-rt^n}) \tag{10}$$

Equation 10 is similar to models suggested by Cil et al. to describe displacement processes.[32] When fitting this model to our data, A_{max}, r, and n are all treated as adjustable parameters.

The porous media micromodel was fabricated from PDMS, which is known to expand when subjected to pressure driven flow.[33] This expansion process introduces flow capacitance which is not captured by the model described in eq 7, hence the need to introduce the variable n to eqs 9 and 10. In the absence of flow capacitance, where $n = 1$, we recover eq 7. Future experiments with less deformable molding materials, such as Norland optical adhesive, will be performed to characterize the role that flow capacitance plays in the displacement process.

3. VALIDATION OF μPIV MEASUREMENTS WITH SIMULATION RESULTS

3.1. Single Phase Flow. Prior to conducting two-phase flow experiments in porous media, a series of single-phase flow experiments were performed and compared to computational fluid dynamics (CFD) results to validate the accuracy of the μPIV experiments. In these experiments, water samples with fluorescent polystyrene tracers were prepared as described in Materials and Methods. The validation experiments were conducted by establishing an equilibrium fluid flow with a flow rate of 150 μL/h. The channel dimension was same as the channel with 70% porosity used in two-phase experiments. The rate of experimental data collection was the same as those described for the two-phase flow experiments. PIVLab was used to extract velocity magnitude and normalized velocity profiles along the direction of flow. Before comparing the experimental and computational results, manual tracking of the fluorescent particles was done using Fiji[34] at several points of the flow field. This step helped improve parameter optimization for accurate μPIV analysis.

The flow field inside the micromodel was resolved using Ansys Fluent 2022 R1 CFD solver. The porous micromodel channel was discretized using Ansys Meshing to generate 291 955 elements with an average element orthogonal quality of 0.98 and a minimum element quality of 0.43. A mesh independency test was performed by changing the mesh size and plotting the velocity magnitude of a specific point in the flow field to ensure that the results were not affected by the element size and grid convergence was achieved, as shown in the Supporting Information. The Navier−Stokes equations were reduced to the Stokes equations for low Reynold's number ($Re \ll 1$) by ignoring the inertial and gravitational terms. Hence, the laminar viscous model was used without gravity effect.

The simulation utilized a boundary condition that established the inlet average velocity to be the volumetric

https://doi.org/10.1021/acsomega.4c04680
ACS Omega 2024, 9, 34070−34080

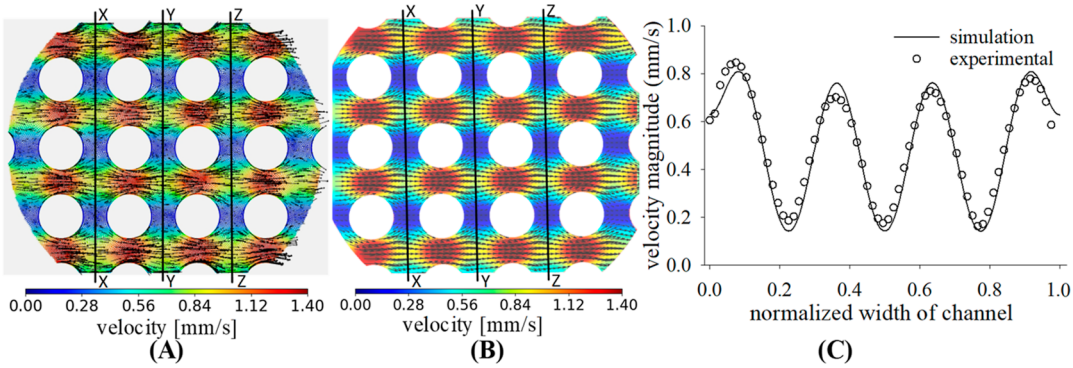

Figure 3. Velocity flow field found from (A) our CFD simulation and (B) our single-phase flow experiment at 150 μL/h. (C) The average velocity magnitude taken at positions *XX*, *YY*, and *ZZ* as shown in (A,B).

flow rate divided by the micromodel cross-sectional area. A gauge pressure of zero (i.e., atmospheric pressure) was applied to the outlet. A pressure-based coupled algorithm was used to solve the velocity in the flow domain. The model used a zero shear stress wall boundary condition to mimic the expected slip that has been observed in hydrophobic microfluidic devices.[35]

The computational and experimental results for single-phase flow are shown in Figure 3A,B, respectively. These results show that the flow velocity is maximum at the pore throat in between the pillars. The flow velocity undergoes a deceleration in the pore spaces, which is consistent with expectations based on the continuity principle and results previously reported in literature.[17] The streamlines form a continuous pattern of converging/diverging flow as the fluid passes through the pores. To quantitatively compare these results, velocity magnitudes were calculated along three profiles, marked *XX*, *YY*, and *ZZ* in Figure 3. The results were averaged and shown in Figure 3C. The computational results show that the maximum predicted velocity is 1.36 mm/s for the conditions simulated. The μPIV data yielded 1.40 mm/s as the maximum velocity. This difference of less than 4% demonstrates the reliability of the μPIV analysis to produce accurate results.

4. RESULTS AND DISCUSSIONS

Three water flow rates were examined for displacement experiments in the micromodels saturated with 25 cSt mineral oil: 37.5, 75, and 150 μL/h. Four realizations for each flow rate were performed. The software package PIVLab was used to extract shear stress distributions and velocity probability density functions (PDFs) for each of these realizations. The water phase saturation and displacement efficiency for each flow rate were found by averaging the results of the four realizations. Each experiment began when the water entered the ROI, and each experiment continued until the saturation curves effectively flattened, indicating that they had reached equilibrium. For 50% porosity, the estimated equilibrium time for flow rates of 37.5, 75, and 150 μL/h are 8.7, 6.2, and 7.12 s, respectively. In 70% porous channel, the estimated equilibrium time for flow rates of 37.5, 75, and 150 μL/h are 9.6, 6.0, and 7.8 s, respectively.

Given the quantity of data collected in our experiments, we have chosen to present two representative experiments in Figures 4 and 5. These figures represent displacement experiments conducted for 150 mL/h in the 50% porosity micromodel (Figure 4) and 70% porosity micromodel (Figure 5). These figures present our μPIV results by showcasing the instantaneous velocity fields in the water phase, the water phase shear stress distributions, and the PDFs of the transverse (i.e., bottom to top) velocity at five different experimental times. The data for other flow rates are available in Supporting Information as Figures S2−S5. The time points shown in Figures 4 and 5 correspond to 20, 40, 60, 80 and 100% of the total time needed to reach equilibrium. The first column of each of these figures show the raw μPIV image associated with the time presented in each row. The fluorescent seed particles dispersed in the water show the instantaneous location of the water phase as it displaces the oil. The second column of these figures shows the shear stress distribution in the water phase as well as the instantaneous velocity field in the water phase. The third column of the figures shows the PDFs of the transverse velocity component for the water phase.

Displacement processes in porous media channels are commonly characterized in terms of mobility ratio (i.e., ratio of oil to water viscosity), wetting/nonwetting surfaces of the media, and flow rates. In the current experiments, the displacement process exhibits a mobility ratio of ∼25, indicating an unfavorable condition as it is much higher than 1. This high ratio leads to fingering, where water protrudes faster through the oil due to lower viscosity, reducing displacement efficiency. Additionally, the oil-wet PDMS surface is likely to pose further unfavorable conditions for oil displacement. When water enters the system, the less viscous water tends to form narrow, finger-like protrusions as it advances through the oil. Over time, the water fingers continue to propagate, creating channels through the oil. These fingers advance unevenly, causing an irregular displacement front. As the water fingers progress, they leave behind large area of trapped oil. Due to the smaller pore sizes in the 50% porous channel compared to 70% porous channel, a larger oil area is left behind since smaller pore sizes contribute to higher capillary pressure posing higher resistance to oil displacement. Eventually, the water fingers reach the outlet of the porous media, marking the breakthrough of water. At this point, a significant portion of the oil remains trapped in the media. Water primarily flows through the established channels, reducing the efficiency of oil displacement. Due to the high mobility ratio and oil-wet nature of PDMS, a considerable amount of oil remains as residual saturation within the porous media. This residual oil is difficult to mobilize without additional enhanced oil recovery techniques.

During the oil displacement experiments, the water phase initially finds a route within the ROI with the least hydraulic resistance and proceeds along that path. The route appears to be the same in subsequent realizations, suggesting that there is

https://doi.org/10.1021/acsomega.4c04680
ACS Omega 2024, 9, 34070−34080

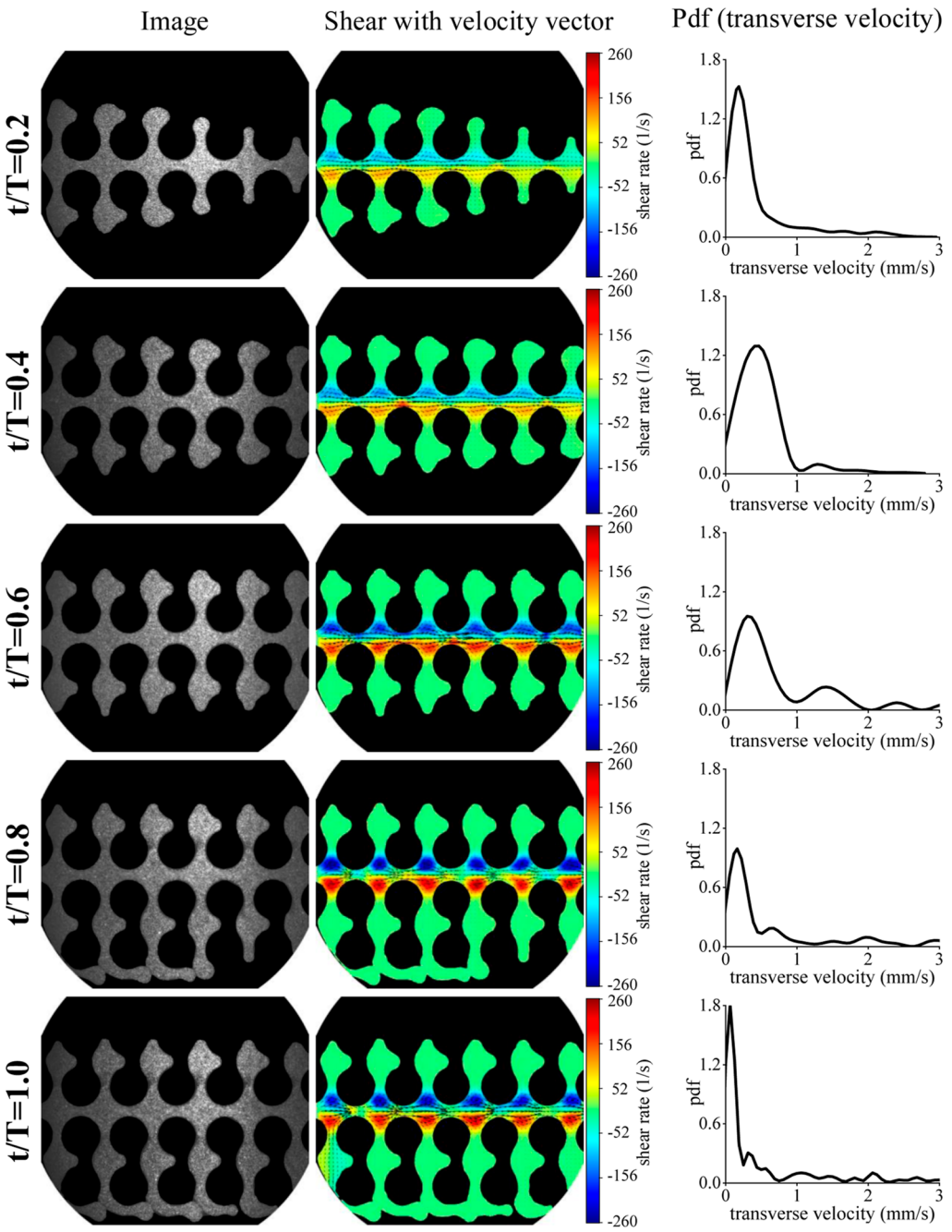

Figure 4. Experimental image (left column), Shear stress distribution (middle column) and PDF (right column) for flow rate of 150 μL/h in 50% porous model.

something inherent in the micromodel that causes the route to be favored. One possibility is that capillary forces acting on fluids in confined spaces cause the water phase to prefer specific parts of the micromodel as it passes through. Evidence for this is observed in the 37.5 μL/h data set for 50% porous model shown in Figure S2, where the water phase penetrates along the micromodel wall. The same phenomenon is observed in Figures S3 and 4 for flow rates of 75 and 150 μL/h, respectively. This observation that wall effects may play a role in determining the path an invading phase follows is consistent with other observations in the literature.[36] The main path that the water phase follows appears to generate branches that propagate along the direction of flow. A similar phenomenon is observed in the 70% porous model as shown in Figures S4, S5, and 5. At the highest flow rate, 150 μL/h, in 70% porous media, the branches appear to coalesce and, eventually, generate a tortuous flow path that returns to the main flow (Figure 5). This behavior reduces oil displacement.

The shear stress distribution serves as an indicator for the displacement process. A shear stress of zero at the oil−water interface indicates that the displacement has reached a local equilibrium. This is particularly evident in pore spaces where the displacing fluid has insufficient momentum for oil displacement. Nonzero shear stresses within the pores indicate that the water phase is either in the process of displacing oil or has achieved dynamic equilibrium whereby the fluid remains in motion as it flows through the porous media. As the water phase enters the porous media, the shear stress is recorded to

https://doi.org/10.1021/acsomega.4c04680
ACS Omega 2024, 9, 34070−34080

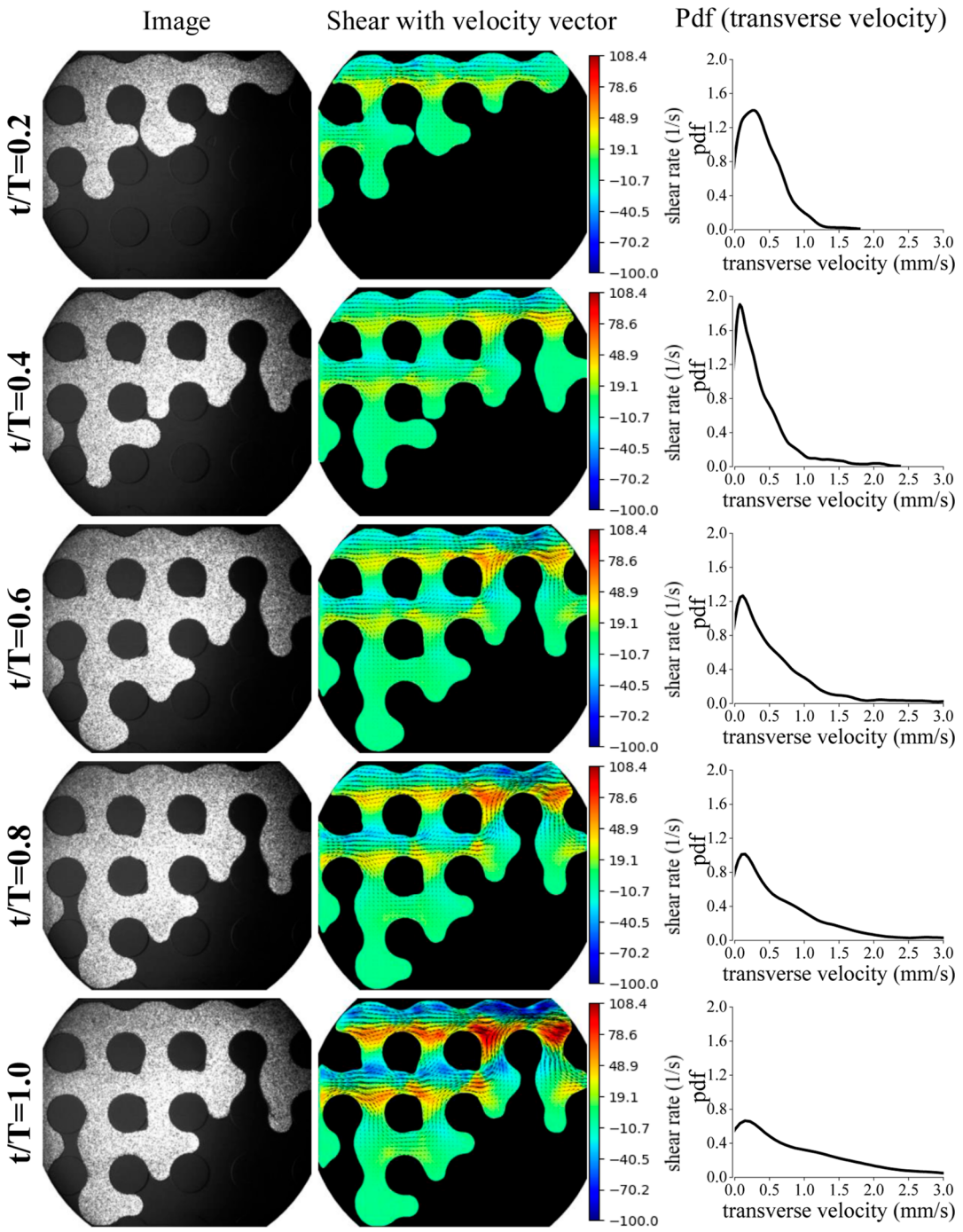

Figure 5. Experimental image (left column), Shear stress distribution (middle column) and PDF (right column) for flow rate of 150 μL/h in 70% porous model.

exhibit low (i.e., near zero) shear stresses, before building up in time. The exception to this observation appears to be 37.5 μL/h in 70% porous channel, where the shear stress fluctuates between low (at t/T = 0.2 and t/T = 0.6) and high magnitudes (t/T = 0.4, t/T = 0.8, and t/T = 1.0). These fluctuations could be indicative of a fluid mode wherein capillary pressure is building until the fluid breaks through. The 50% porous channel always produced significantly higher shear rates than in the 70% porous channel. In 50% porous channel, the 37.5 μL/h flow rate achieved a maximum shear rate of 45.0 s^{-1}, whereas the 75, and 150 μL/h flow rates had shear rates of 70.0 and 260.0 s^{-1}, respectively. In 70% porous channel, the 37.5 μL/h flow rate achieved a maximum shear rate of 12.0 s^{-1}, whereas the 75, and 150 μL/h flow rates had shear rates of 35.85 and 108.4 s^{-1}, respectively. At the higher flow rates, the back pressure may be sufficient to break the viscous resistance of the oil.

PDFs were constructed to help characterize the distribution of the velocity data. The transverse velocity was chosen for this analysis as it was found that this velocity component provides insight into predicting the oil displacement by the water phase. These data show that the transverse velocity distribution is initially broad. For example, in Figure S2 for 50% porous case, the PDF of transverse velocity for the flow rate of 37.5 μL/h

https://doi.org/10.1021/acsomega.4c04680
ACS Omega 2024, 9, 34070−34080

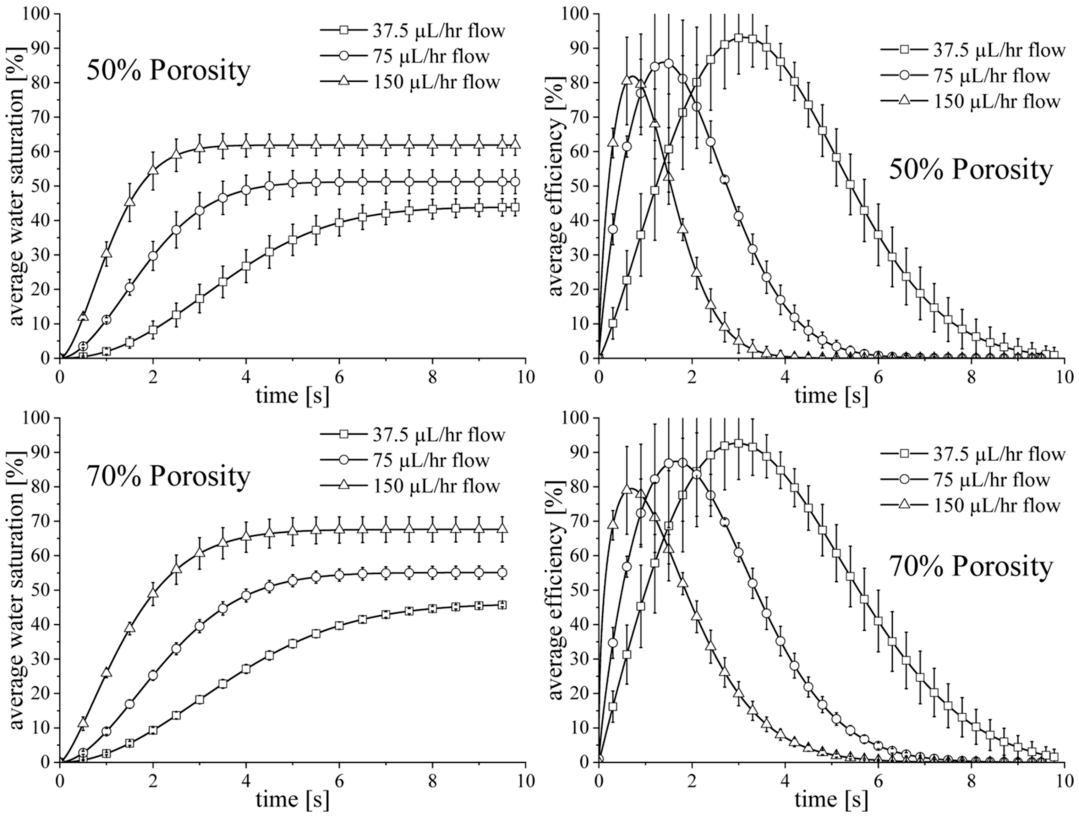

Figure 6. Average water saturations (left column) and average efficiencies (right column) of four realizations for 50% (top row) and 70% porosity (bottom row).

shows that the transverse velocity has a distribution of magnitudes that vary from 0 to 0.25 mm/s, with a peak (i.e., most probable) magnitude of ∼0.015 mm/s for the t/T = 0.2 time frame. The PDF for this flow rate broadens at t/T = 0.4, with a corresponding reduction of the probability of the peak probability. At t/T = 0, the higher pdf values in a bigger range of transverse velocity indicate higher oil displacement. As time increases, the transverse velocity at the peak probability continues to decrease, indicating a decrease in the rate of oil displacement, as the water no longer moves vertically into oil-containing regions. After t/T = 1.0, the peak probability transverse velocity is 0 mm/s, indicating that the water has stopped displacing the oil within the ROI. The flow rate of 75 and 150 μL/h exhibit behavior that is similar to the 37.5 μL/h case. Similar trend is observed in the case of 70% porous channel, except for 150 μL/h, which exhibits a PDF peak value at ∼0.25 mm/s with a maximum value of 3 mm/s. This deviation is the result of the coalescence and tortuosity behavior described above for this flow rate.

The PDFs provide insight into when a displacement process has achieved equilibrium, but as we see from the 150 μL/h case in 70% porous channel, there are exceptions to the behavior of this process. Thus, it is also informative to examine the saturation curves based on eq 10. This is done by using video data to calculate the area occupied by the invading water phase as a function of time. The displacement process eventually reaches a point where the area occupied by the water phase is maximum (i.e., A_{max}) and is unable to displace additional oil. Figure 6 (left) shows the results from this analysis. In Figure 6 (left), the total area displaced by the water phase, $A_w(t)$, is normalized by the ROI area (i.e., the image area) to determine the degree of water saturation. The curves represent averages over four separate realizations for each flow rate. The maximum water saturation for the flow rates of 37.5, 75, and 150 μL/h are approximately 42, 51 and 62%, respectively for the 50% porous channel. Whereas the maximum water saturation for the flow rates of 37.5, 75, and 150 μL/h are approximately 46, 55 and 67.5%, respectively for the 70% porous channel. Higher flow rates produced higher water saturation due to higher kinetic energy of water carrying the ability to overcome capillary forces. Though water saturation is higher at higher flow rates, higher flow rates disproportionately raise the energy and volume of water required to displace each unit of oil. The 70% porous channel had higher water saturation than the 50% porous channel in all flow rates. This is since smaller pores pose more resistance to oil displacement as water needs to overcome higher capillary pressure and lower relative permeability. Moreover, 50% porosity and 70% porosity have similar efficiency profiles due to similar pore connectivity providing similar displacement mechanisms. The data show that the lowest flow rate examined in this study exhibits very little variation between realizations in the 70% porous channel. The variation as measured by the standard deviation of the data appears to increase with flow rate in the 70% porous channel. However, standard deviations are similar for all flow rates for the 50% porous channel.

The saturation curves in Figure 6 (left) can be converted into a displacement efficiency by using the definition in eq 8 and the modified definition of water displacement rate (eq 9)

$$\varepsilon = \frac{hnrt^{n-1}}{Q}(A_{max} - A_w) \tag{11}$$

https://doi.org/10.1021/acsomega.4c04680
ACS Omega 2024, 9, 34070−34080

Table 2. Parameters Used to Fit eqs 9−11 to Measured Oil Displacement in 50% Porous Model

			parameter values			
parameters	equations	flow rates (Q, μL/h)	realization 1	realization 2	realization 3	realization 4
A_{max} (mm^2)	9−11	37.5	1.014	0.807	0.887	0.804
		75	0.852	0.967	0.854	1.16
		150	1.182	0.9407	1.186	1.196
r (1/s)	9−11	37.5	0.03956	0.02241	0.1038	0.0174
		75	0.24	0.2717	0.2526	0.22
		150	0.4491	0.5708	0.8571	0.81
n	9−11	37.5	2.073	2.351	2.021	2.272
		75	1.65	1.474	1.639	2.5
		150	1.426	1.2	2.16	1.813

Table 3. Parameters Used to Fit eqs 9−11 to Measured Oil Displacement in 70% Porous Model

			parameter values			
parameters	equations	flow rates (Q, μL/h)	realization 1	realization 2	realization 3	realization 4
A_{max} (mm^2)	9−11	37.5	0.933	0.976	0.98	0.99
		75	1.227	1.134	1.22	1.202
		150	1.625	1.587	1.419	1.401
r (1/s)	9−11	37.5	0.0464	0.0619	0.05505	0.06682
		75	0.1685	0.1991	0.1918	0.1468
		150	0.451	0.4078	0.5321	0.54
n	9−11	37.5	2.05	1.92	2.03	1.9
		75	1.699	1.655	1.845	1.94
		150	1.664	1.482	1.247	1.246

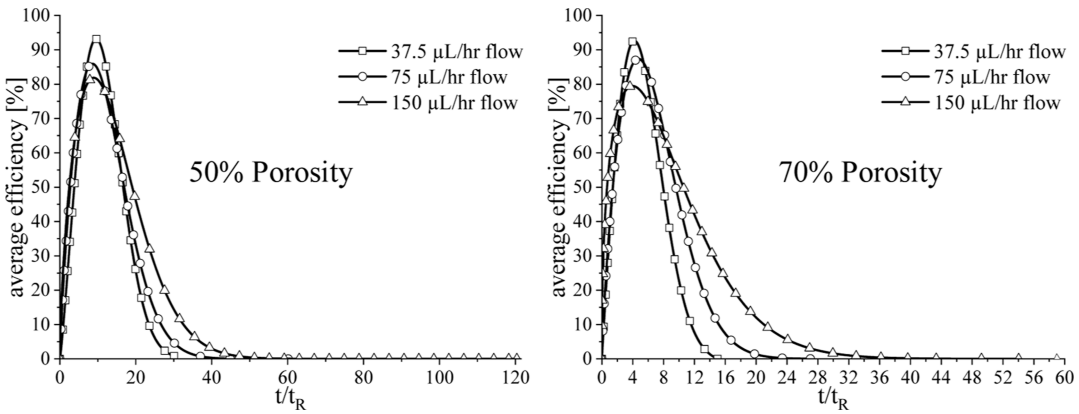

Figure 7. Efficiency variation with normalized time (with respect to residence time t_R) for 50% (left) and 70% porosities (right).

Note that by this definition, a displacement efficiency of 100% means that a given volume of injected water displaces an equal volume of mineral oil. The parameters found from fitting eq 11 to data in Figure 6 (left) are in Table 2 for the 50% porous channel, and Table 3 for the 70% porous channel. These results are used to plot the efficiency curves shown in Figure 6 (right). The peak efficiency for the flow rates of 37.5, 75, and 150 μL/h are 93, 86, and 82%, respectively for the 50% porous channel. The peak efficiency for the flow rates of 37.5, 75, and 150 μL/h are 93, 87, and 80%, respectively for the 70% porous channel.

The dynamic processes in terms of shear stress distribution and PDF distribution of transverse velocities can be related to the efficiency profiles. At the onset of water injection into the channel, both shear stress and displacement efficiency are initially low due to insufficient hydrodynamic forces needed to mobilize a significant volume of oil. As water progressively displaces oil, the shear stress escalates, indicative of increased interfacial interactions, thereby enhancing displacement efficiency until it reaches a maximum. Beyond this peak, although shear stress remains elevated, efficiency declines. This suggests that the water encounters increased resistance as the more readily displaceable oil has already been mobilized, leaving behind oil that requires greater energy for extraction, thus diminishing efficiency. In terms of transverse velocity distribution, initially, the PDF for transverse velocity is broad, encompassing lower transverse velocities which facilitates oil displacement at a modest rate. With ongoing water injection, the PDF expands to include higher transverse velocities, correlating with enhanced displacement efficiency that eventually peaks. Subsequently, the PDF narrows toward lower velocities and approaches zero, signifying a reduction in transverse velocity. This narrowing of the velocity distribution corresponds to a decrease in efficiency, which ultimately reaches zero when the system achieves equilibrium.

https://doi.org/10.1021/acsomega.4c04680
ACS Omega 2024, 9, 34070−34080

To observe if there are any commonalities between the displacement efficiency data in Figure 6 (right), the time axis was rescaled by using residence time as a normalization factor. Residence time is defined as $t_R = V_p/Q$, where V_p is the pore volume. By introducing this normalization to the displacement efficiency data, shown in Figure 7 (left), one finds that the displacement efficiency appears to peak around $t/t_R \approx 9$ for all flow rates in the 50% porous channel. However, as shown in Figure 7 (right), displacement efficiency appears to peak around $t/t_R \approx 4$ for all flow rates in the 70% porous channel. This suggests that the displacement process observed in the experiments appears to peak once nine, and four pore volumes have been displaced in the 50%, and the 70% micromodels, respectively. The time required to reach these peaks at $t/t_R \approx 4$ and $t/t_R \approx 9$ likely represents the capacitance time for the system (i.e., the time required for the channel and inlet tubing to expand to their greatest extent). In a rigid channel with rigid inlet tubing, maximum displacement of oil would begin right away, as any water entering the system must immediately displace any oil present due to conservation of mass. However, in this system, some of the water entering the system at early times displaces the expanding volume and not the oil, hence the reduced oil displacement until the expansion reaches maximum value.

Based on the data for the 50% porous channel, the 37.5 μL/h oil displacement rate approaches zero when $t/t_R \approx 30$. The convergence time required to reach this equilibrium for the 75 μL/h flow rate is double that of 37.5 μL/h at $t/t_R \approx 60$. The equilibrium time doubles again to $t/t_R \approx 120$ for 150 μL/h. Similar phenomenon is found for the 70% porous channel with convergence times of 15, 30, and 60 for 37.5, 75, and 150 μL/h flow rates, respectively.

5. CONCLUSIONS

This work examines the application of microscopic particle image velocimetry (μPIV) to the investigation of oil phase displacement by a water phase in a porous media micromodel. This investigation characterized the displacement behavior of three flow rates in micromodels with porosities of 0.5 and 0.7. It was observed that the invading water phase would follow similar paths across all experimental realizations. This suggests that wall effects within confined spaces are acting to direct the flow along specific paths. The shear stress exhibited by the invading water phase begins with a low value before increasing over time to achieve a maximum value once equilibrium is achieved. The exception to this observation occurred at a flow rate of 37.5 μL/h in the 70% porous channel, which appeared to undergo fluctuations that could be indicative of fluctuations in capillary pressure. Distributions obtained from PDFs of transverse velocity indicate that the transverse velocity is an excellent indicator of when an invading fluid has reached the equilibrium condition. In particular, a PDF peak probability of 0 mm/s is observed when the oil-phase displacement has reached equilibrium. This trend does not appear to hold for 150 μL/h in the 70% porous channel, which exhibits a PDF peak value at ~0.25 mm/s, which results from the coalescence of fluid branches that expand from the main flow.

The authors developed a simple model based on mass conservation, which was modified to describe the water-phase saturation. This model deviates from the expected form, likely as a result of flow capacitance in the micromodel channels. Based on this model, the authors propose displacement efficiency as a metric to describe the effectiveness of the displacement process. Examining displacement efficiency and residence time, it was found that the displacement efficiency peaks after the displacement of ~9 pore volumes and ~4 pore volumes for the 50%, and the 70% porous channels, respectively. This observation appears to hold for all the flow rates examined here. The time it takes to reach peak displacement is likely the result of flow capacitance, which represents the time it takes for the channel walls and tubing to expand in response to the displacement process. The use of a more rigid material in the micromodels could influence these results and will be examined in future work. The experimental results described here can be applied to a variety of porous media displacement processes from the extraction of natural resources to chemical processing in packed bed reactors.

■ ASSOCIATED CONTENT

Supporting Information

The Supporting Information is available free of charge at https://pubs.acs.org/doi/10.1021/acsomega.4c04680.

Grid independency test (Figure S1). Shear stress distribution and PDF for flow rate of 37.5 μL/h in the 50% porous model (Figure S2). Shear stress distribution and PDF for flow rate of 75 μL/h in the 50% porous model (Figure S3). Shear stress distribution and PDF for flow rate of 37.5 μL/h in the 70% porous model (Figure S4). Shear stress distribution and PDF for flow rate of 75 μL/h in the 70% porous model (Figure S5) (PDF)

■ AUTHOR INFORMATION

Corresponding Authors

Michael G. Olsen − *Department of Mechanical Engineering, Iowa State University, Ames, Iowa 50011, United States*; Email: mgolsen@iastate.edu

Jaime J. Juárez − *Department of Mechanical Engineering, Iowa State University, Ames, Iowa 50011, United States*; orcid.org/0000-0002-4719-3896; Email: jjuarez@iastate.edu

Authors

Md. Abdul Karim Miah − *Department of Mechanical Engineering, Iowa State University, Ames, Iowa 50011, United States*

Kawkab Ahasan − *Department of Mechanical Engineering, Iowa State University, Ames, Iowa 50011, United States*

Todd A. Kingston − *Department of Mechanical Engineering, Iowa State University, Ames, Iowa 50011, United States*; orcid.org/0000-0003-4981-4884

Complete contact information is available at: https://pubs.acs.org/10.1021/acsomega.4c04680

Notes

The authors declare no competing financial interest.

■ ACKNOWLEDGMENTS

J.J.J. and M.G.O. gratefully acknowledge the support of the United States National Science Foundation through award number 2050105.

■ REFERENCES

(1) Skauge, A.; Zamani, N.; Gausdal Jacobsen, J.; Shaker Shiran, B.; Al-Shakry, B.; Skauge, T. Polymer Flow in Porous Media: Relevance to Enhanced Oil Recovery. *Colloids Interfaces* **2018**, *2* (3), 27.

(2) Pesavento, F.; Schrefler, B. A.; Sciumè, G. Multiphase Flow in Deforming Porous Media: A Review. *Arch. Comput. Methods Eng.* **2017**, *24* (2), 423−448.
(3) Shu, X.; Wu, Y.; Zhang, X.; Yu, F. Experiments and Models for Contaminant Transport in Unsaturated and Saturated Porous Media − A Review. *Chem. Eng. Res. Des.* **2023**, *192*, 606−621.
(4) Rizzo, C. B.; de Barros, F. P. J. Minimum Hydraulic Resistance and Least Resistance Path in Heterogeneous Porous Media. *Water Resour. Res.* **2017**, *53* (10), 8596−8613.
(5) Lu, X.; Zhao, Y.; Dennis, D. J. C. Flow Measurements in Microporous Media Using Micro-Particle Image Velocimetry. *Phys. Rev. Fluids* **2018**, *3* (10), 104202.
(6) Xu, W.; Ok, J. T.; Xiao, F.; Neeves, K. B.; Yin, X. Effect of Pore Geometry and Interfacial Tension on Water-Oil Displacement Efficiency in Oil-Wet Microfluidic Porous Media Analogs. *Phys. Fluids* **2014**, *26* (9), 093102.
(7) Chatenever, A.; Calhoun, J. C. Visual Examinations of Fluid Behavior in Porous Media - Part I. *J. Pet. Technol.* **1952**, *4* (06), 149−156.
(8) Yeh, H.-L.; Juárez, J. J. Ultrasound-Enhanced Diffusion and Streaming of Colloids in Porous Media. *Exp. Therm. Fluid Sci.* **2021**, *121*, 110282.
(9) He, K.; Babaye Khorasani, F.; Retterer, S. T.; Thomas, D. K.; Conrad, J. C.; Krishnamoorti, R. Diffusive Dynamics of Nanoparticles in Arrays of Nanoposts. *ACS Nano* **2013**, *7* (6), 5122−5130.
(10) Vavra, E. D.; Zeng, Y.; Xiao, S.; Hirasaki, G. J.; Biswal, S. L. Microfluidic Devices for Characterizing Pore-Scale Event Processes in Porous Media for Oil Recovery Applications. *J. Visualized Exp.* **2018**, *131*, No. e56592.
(11) Northrup, M. A.; Kulp, T. J.; Angel, S. M. Fluorescent Particle Image Velocimetry: Application to Flow Measurement in Refractive Index-Matched Porous Media. *Appl. Opt.* **1991**, *30* (21), 3034−3040.
(12) Krummel, A. T.; Datta, S. S.; Münster, S.; Weitz, D. A. Visualizing Multiphase Flow and Trapped Fluid Configurations in a Model Three-Dimensional Porous Medium. *AIChE J.* **2013**, *59* (3), 1022−1029.
(13) Li, L.; Iskander, M. Visualization of Interstitial Pore Fluid Flow. *J. Imaging* **2022**, *8* (2), 32.
(14) Roman, S.; Soulaine, C.; AlSaud, M. A.; Kovscek, A.; Tchelepi, H. Particle Velocimetry Analysis of Immiscible Two-Phase Flow in Micromodels. *Adv. Water Resour.* **2016**, *95*, 199−211.
(15) Heshmati, M.; Piri, M. Interfacial Boundary Conditions and Residual Trapping: A Pore-Scale Investigation of the Effects of Wetting Phase Flow Rate and Viscosity Using Micro-Particle Image Velocimetry. *Fuel* **2018**, *224*, 560−578.
(16) Zarikos, I.; Terzis, A.; Hassanizadeh, S. M.; Weigand, B. Velocity Distributions in Trapped and Mobilized Non-Wetting Phase Ganglia in Porous Media. *Sci. Rep.* **2018**, *8* (1), 13228.
(17) Blois, G.; Barros, J. M.; Christensen, K. T. A Microscopic Particle Image Velocimetry Method for Studying the Dynamics of Immiscible Liquid−Liquid Interactions in a Porous Micromodel. *Microfluid. Nanofluid.* **2015**, *18* (5−6), 1391−1406.
(18) Bultreys, T.; Van Offenwert, S.; Goethals, W.; Boone, M. N.; Aelterman, J.; Cnudde, V. X-Ray Tomographic Micro-Particle Velocimetry in Porous Media. *Phys. Fluids* **2022**, *34* (4), 042008.
(19) Haffner, E. A.; Mirbod, P. Velocity Measurements of Dilute Particulate Suspension over and through a Porous Medium Model. *Phys. Fluids* **2020**, *32* (8), 083608.
(20) Holdich, R. G. *Fundamentals of Particle Technology*; Midland Information Technology & Publishing: Shepshed, 2002.
(21) Huang, E.; Skoufis, A.; Denning, T.; Qi, J.; Dagastine, R. R.; Tabor, R. F.; Berry, J. D. OpenDrop: Open-Source Software for Pendant Drop Tensiometry & Contact Angle Measurements. *J. Open Source Softw.* **2021**, *6* (58), 2604.
(22) Berry, J. D.; Neeson, M. J.; Dagastine, R. R.; Chan, D. Y. C.; Tabor, R. F. Measurement of Surface and Interfacial Tension Using Pendant Drop Tensiometry. *J. Colloid Interface Sci.* **2015**, *454*, 226−237.
(23) Chen, H.; Muros-Cobos, J. L.; Holgado-Terriza, J. A.; Amirfazli, A. Surface Tension Measurement with a Smartphone Using a Pendant Drop. *Colloids Surf., A* **2017**, *533*, 213−217.
(24) Sobera, M. P.; Kleijn, C. R. Hydraulic Permeability of Ordered and Disordered Single-Layer Arrays of Cylinders. *Phys. Rev. E* **2006**, *74* (3), 036301.
(25) Thielicke, W.; Stamhuis, E. J. PIVlab − Towards User-Friendly, Affordable and Accurate Digital Particle Image Velocimetry in MATLAB. *J. Open Res. Softw.* **2014**, *2* (1), 30.
(26) Thielicke, W.; Sonntag, R. Particle Image Velocimetry for MATLAB: Accuracy and Enhanced Algorithms in PIVlab. *J. Open Res. Softw.* **2021**, *9*, 12.
(27) Bourdon, C. J.; Olsen, M. G.; Gorby, A. D. Power-Filter Technique for Modifying Depth of Correlation in microPIV Experiments. *Exp. Fluids* **2004**, *37* (2), 263−271.
(28) Bourdon, C. J.; Olsen, M. G.; Gorby, A. D. Validation of an Analytical Solution for Depth of Correlation in Microscopic Particle Image Velocimetry. *Meas. Sci. Technol.* **2004**, *15* (2), 318−327.
(29) Olsen, M. G.; Adrian, R. J. Out-of-Focus Effects on Particle Image Visibility and Correlation in Microscopic Particle Image Velocimetry. *Exp. Fluids* **2000**, *29* (7), S166−S174.
(30) Yeh, H.-L.; Juarez, J. J. Oil Phase Displacement by Acoustic Streaming in a Reservoir-on-a-Chip. *Microfluid. Nanofluid.* **2019**, *23* (10), 113.
(31) Aarnes, J. E.; Gimse, T.; Lie, K.-A. An Introduction to the Numerics of Flow in Porous Media Using Matlab. In *Geometric Modelling, Numerical Simulation, and Optimization*; Applied Mathematics at SINTEF, 2007.
(32) Cil, M.; Reis, J. C.; Miller, M. A.; Misra, D. *An Examination of Countercurrent Capillary Imbibition Recovery from Single Matrix Blocks and Recovery Predictions by Analytical Matrix/Fracture Transfer Functions*; Society of Petroleum Engineers, 1998.
(33) Gervais, T.; El-Ali, J.; Günther, A.; Jensen, K. F. Flow-Induced Deformation of Shallow Microfluidic Channels. *Lab Chip* **2006**, *6* (4), 500−507.
(34) Schindelin, J.; Arganda-Carreras, I.; Frise, E.; Kaynig, V.; Longair, M.; Pietzsch, T.; Preibisch, S.; Rueden, C.; Saalfeld, S.; Schmid, B.; Tinevez, J.-Y.; White, D. J.; Hartenstein, V.; Eliceiri, K.; Tomancak, P.; Cardona, A. Fiji: An Open-Source Platform for Biological-Image Analysis. *Nat. Methods* **2012**, *9* (7), 676−682.
(35) Berg, S.; Cense, A. W.; Hofman, J. P.; Smits, R. M. M.; Rijswijk, G. *Flow in Porous Media With Slip Boundary Condition*; International Symposium of the Society of Core Analysts, 2007.
(36) Yiotis, A.; Karadimitriou, N. K.; Zarikos, I.; Steeb, H. Pore-Scale Effects during the Transition from Capillary- to Viscosity-Dominated Flow Dynamics within Microfluidic Porous-like Domains. *Sci. Rep.* **2021**, *11* (1), 3891.

https://doi.org/10.1021/acsomega.4c04680
ACS Omega 2024, 9, 34070−34080